Mitotic Outcomes and Errors in Fibrous Environments

Aniket Jana[1], Apurba Sarkar[2], Haonan Zhang[1], Atharva Agashe[1], Ji Wang[3], Raja Paul[2], Nir S. Gov[4], Jennifer G. DeLuca[5], Amrinder S. Nain[1,3*]

[1] Department of Mechanical Engineering, Virginia Tech, Blacksburg, VA 24061, USA
[2] School of Mathematical and Computational Sciences, Indian Association for the Cultivation of Science, Jadavpur, Kolkata, 700032, India
[3] Department of Biomedical Engineering and Mechanics, Virginia Tech, Blacksburg, VA 24061, USA
[4] Department of Chemical and Biological Physics, Weizmann Institute of Science, Rehovot, 7610001, Israel
[5] Department of Biochemistry and Molecular Biology, Colorado State University, Fort Collins, CO 80523, USA

***corresponding author: nain@vt.edu**

SUPPORTING INFORMATION

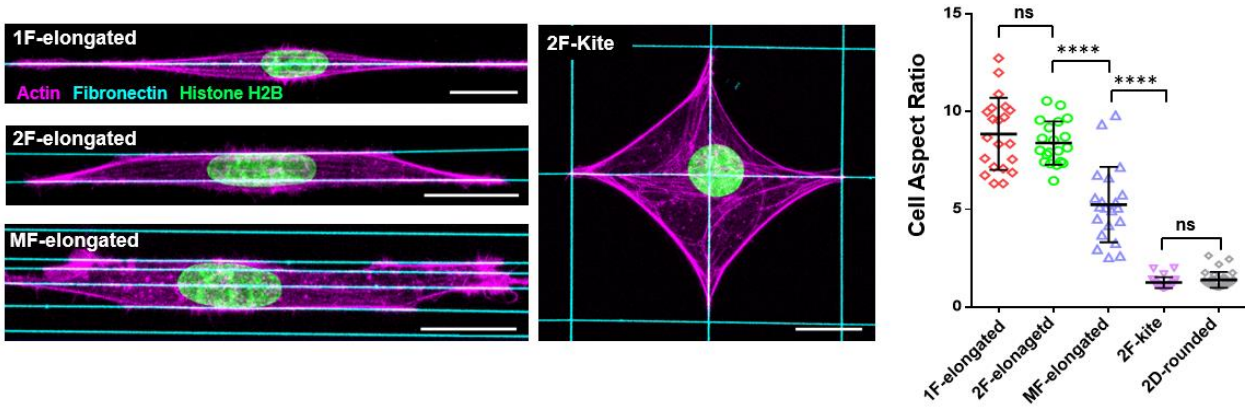

Fig. S1. Cell shapes during Interphase. Representative stained images and cell aspect ratio quantification corresponding to 1F-elongated, 2F-elongated, MF-elongated, 2F-kite and 2D-rounded. Scale bar 10 µm.

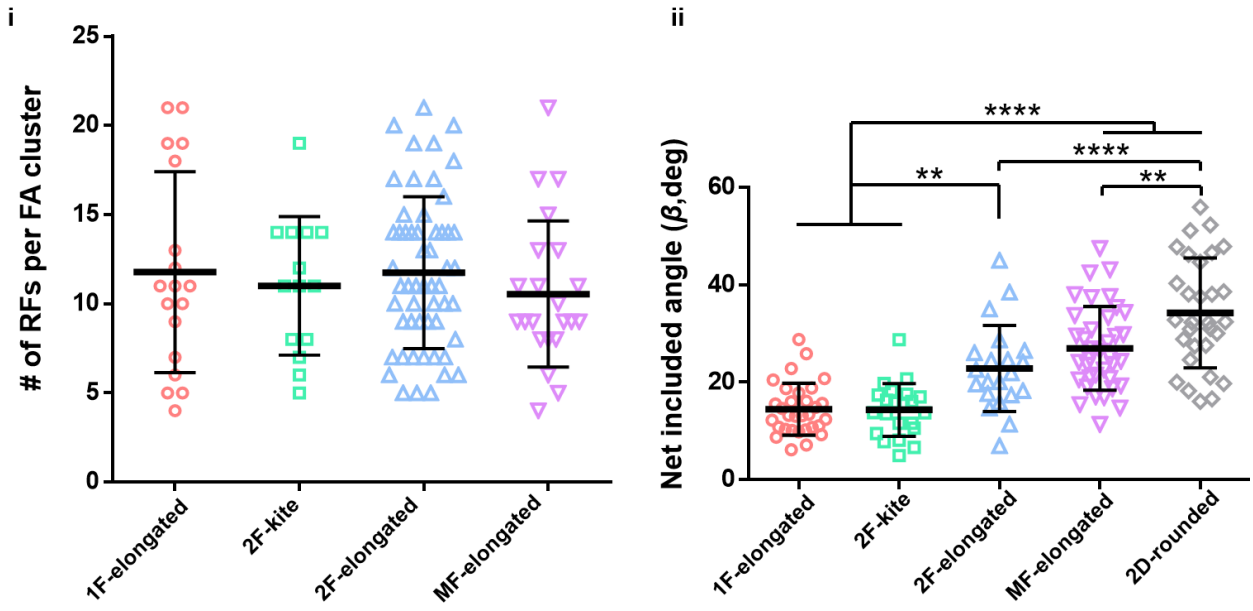

Fig. S2. Quantification of number and arrangement of retraction fibers associated with each focal adhesion cluster for the different cell shapes. (i) Number of retraction fibers per FA cluster across all cell shapes, and (ii) the angle made by retraction fibers from adhesion sites on fibers to attachment on cell cortex.

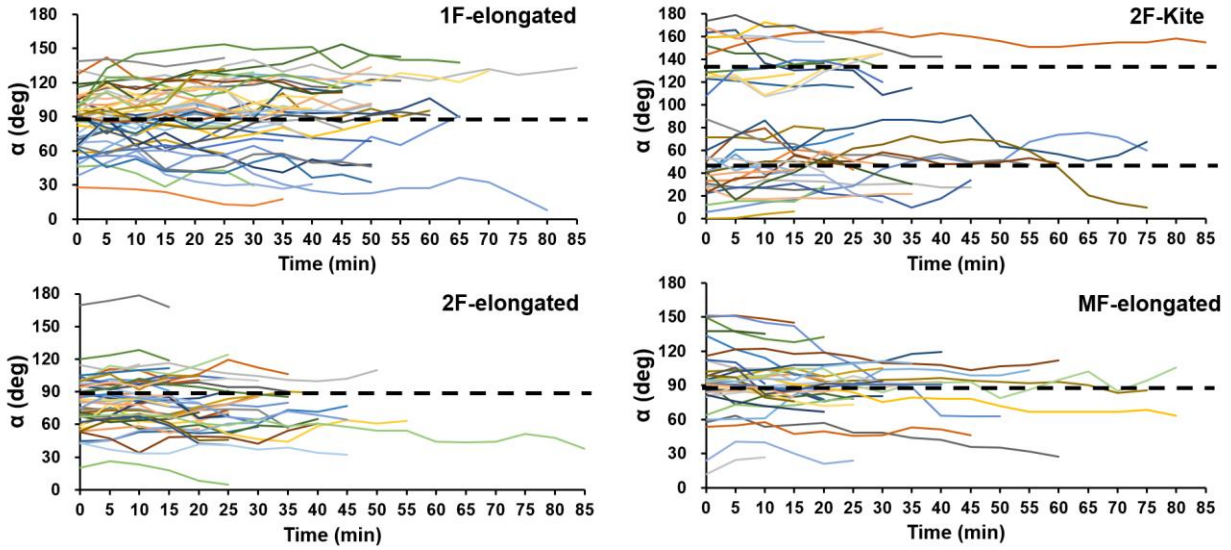

Fig. S3. Compilation of individual profiles showing temporal dynamics of metaphase plate movements for the different fiber geometries.

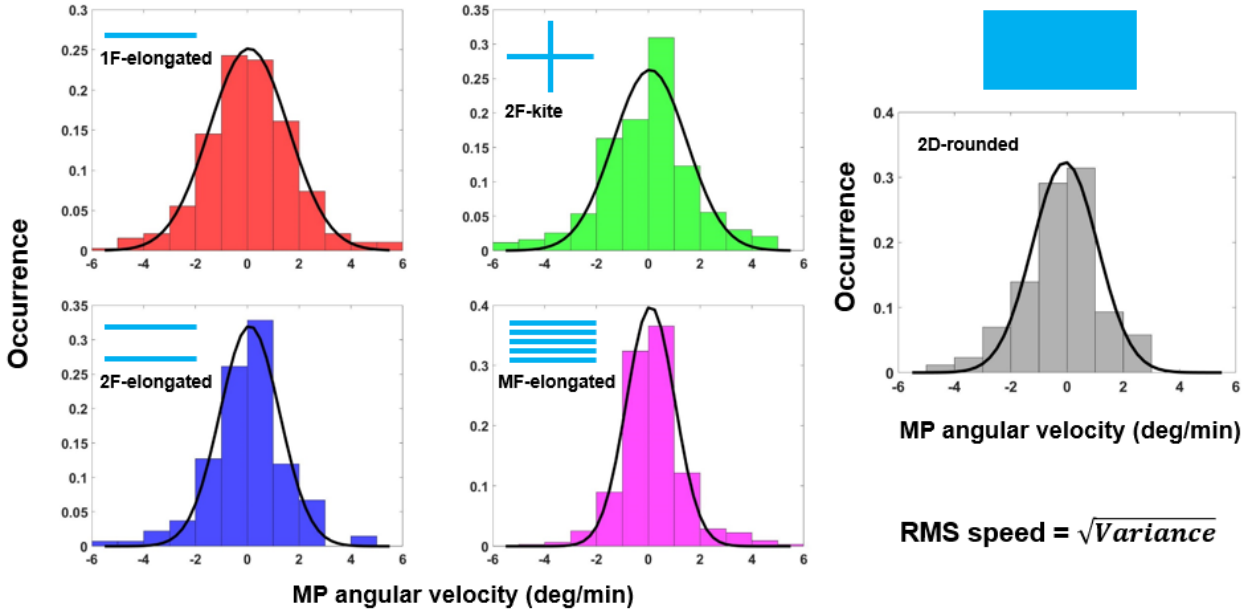

Fig. S4. Probability distributions of the metaphase plate angular velocity for the different substrate categories.

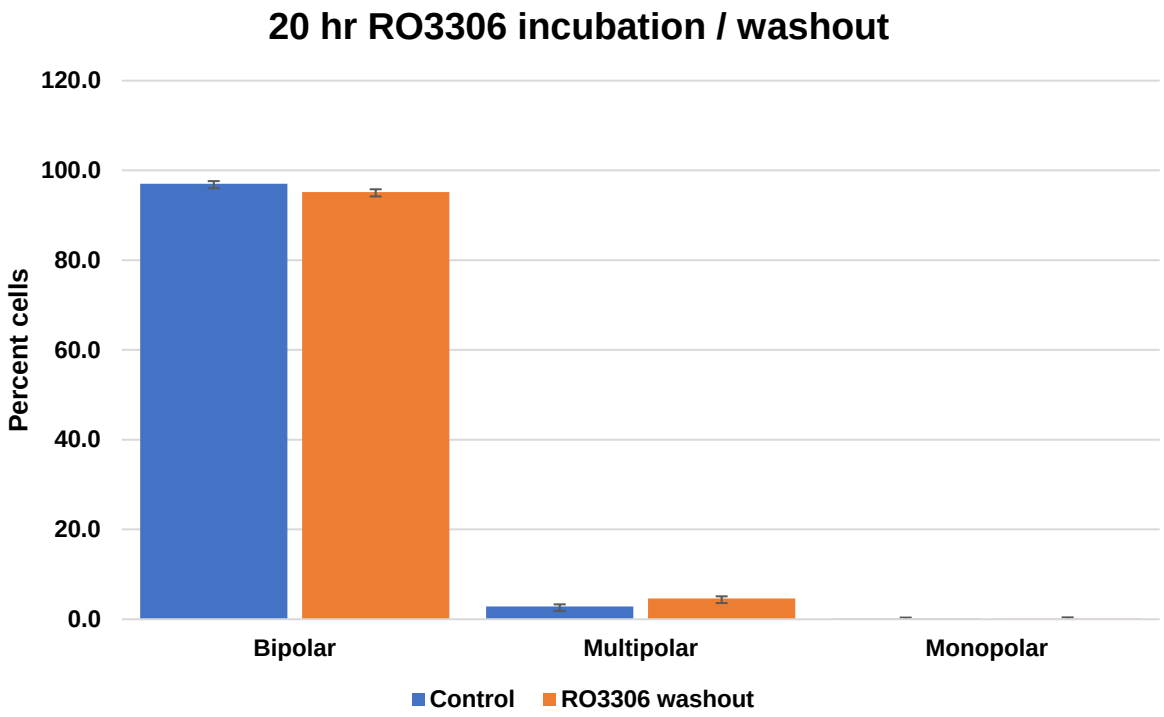

Fig. S5. Spindle polarity phenotypes in control cells and cells treated with the Cdk1 inhibitor RO-3306. Asynchronous HeLa cells expressing H2B-GFP were treated with DMSO (control vehicle) or RO-3306 for 20 hours. Cells were then released from RO-3306 by washing cells with drug-free media for 30 min (total of 6 X 5 min washes). Cells were fixed, immunostained with anti-tubulin antibodies, and subsequently imaged and analyzed. For each condition, 3 independent experiments were carried out, and at least 100 cells were measured from each experiment. For each paired comparison, $p<0.001$.

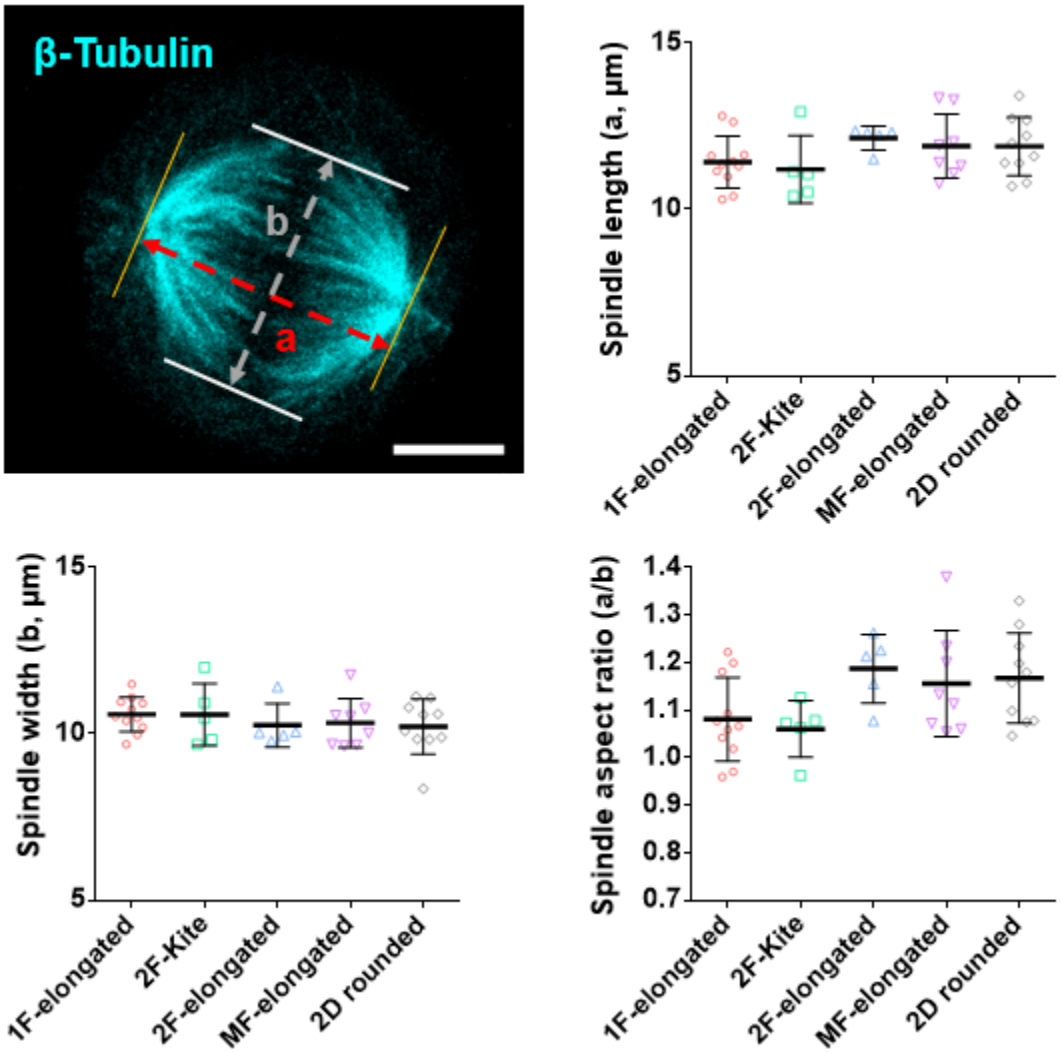

Fig. S6. Comparison of mitotic spindle shape over different substrate categories. The length and width of the mitotic spindle is shown by a and b in the representative stained image. Aspect ratio is defined as a/b, scale bar is 5 µm.

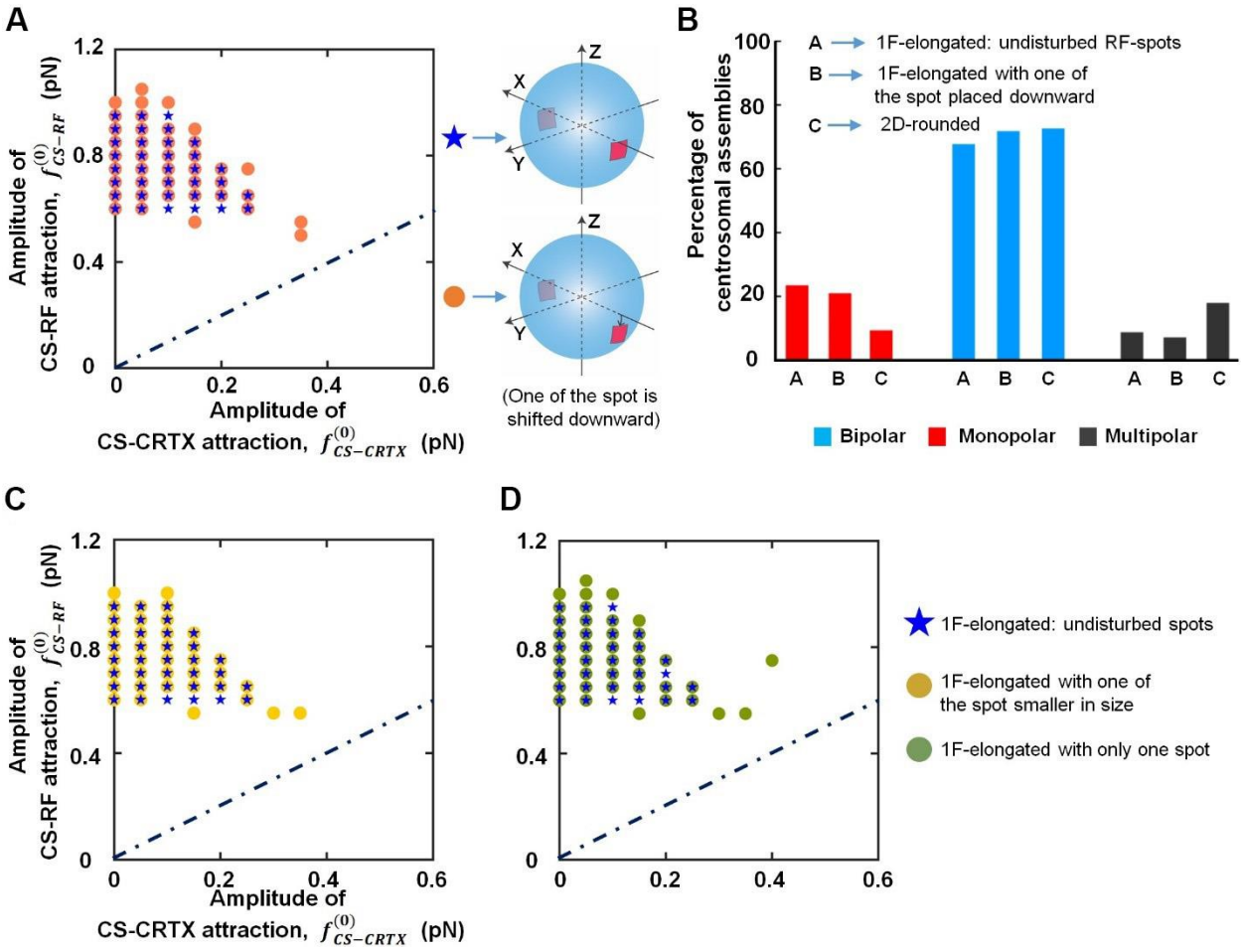

Fig. S7. The CS-CRTX and CS-RF attraction parameters satisfy the observations for 1F-elongated and 2D-rounded cases, and are insensitive to variations in RF-geometry in the 1F-elongated case. One of the RF spots in the 1F-elongated configuration shifted downward or decreased in size. The RF distributions for the 2D scenario are unchanged. (*A*) The data compares the outcomes if one of the RF spots in the 1F-elongated scenario is shifted downward by 20^0 from the equatorial plane or left undisturbed. For one such parameter combination ($f^{(0)}_{CS-CRTX} = 0.1\ pN$ and $f^{(0)}_{CS-RF} = 0.75\ pN$), the corresponding statistics of mono-, bi-, and multipolar spindles are illustrated in (*B*). When compared to the unaltered spot sizes in the 1F-elongated case, the changes are insignificant in the experimentally favorable parameter regimes if one of the spot sizes is smaller (~ half of the other) (*C*) or zero (*D*).

Spindle outcomes are strongly influenced by the RF distributions in the 2D-rounded scenario:

Unlike the 1F-elongated case, the 2D-rounded scenario strongly influences the spindle outcomes due to its significantly broader band-like distributions of the RF regions. Tweaking the size and position of one of the spots in the 1F-elongated configuration has no discernible effect on the parameter regimes corresponding to the experimental predictions (**Fig. S7**). However, increasing or decreasing the width of the RF band in the 2D-rounded scenario results in an overall downward or upward shift in the experimentally consistent parameter regimes (**Fig. S8**). This implies that a stronger or weaker pull from the RF band is required to achieve experimentally consistent results with altered RF bandwidth.

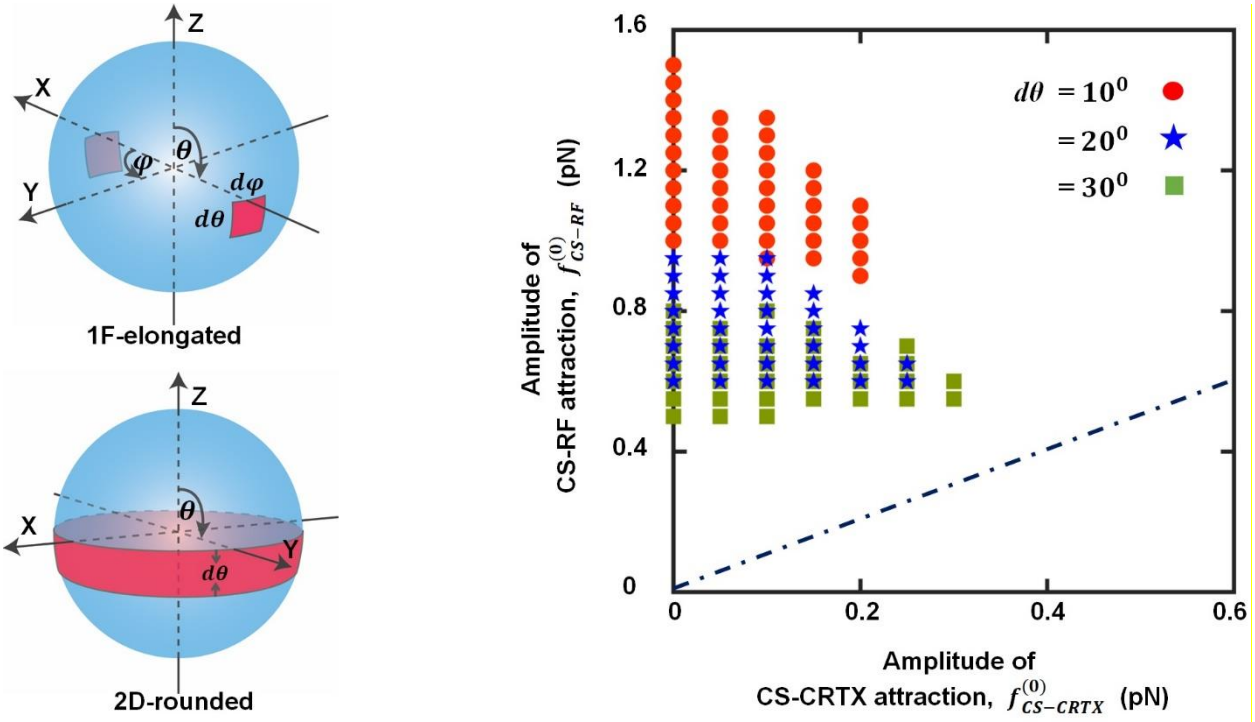

Fig. S8. Experimentally consistent parameter regimes are dependent on the width of the RF-band in the 2D-rounded case. The joint parameter space satisfying the experimental results for the 1F-elongated and 2D-rounded cases are shown with three different RF-spots/band widths: $d\theta = 10^0$, 20^0, and 30^0, respectively. Note that $d\varphi = d\theta$ for the RF spots in the 1F-elongated case.

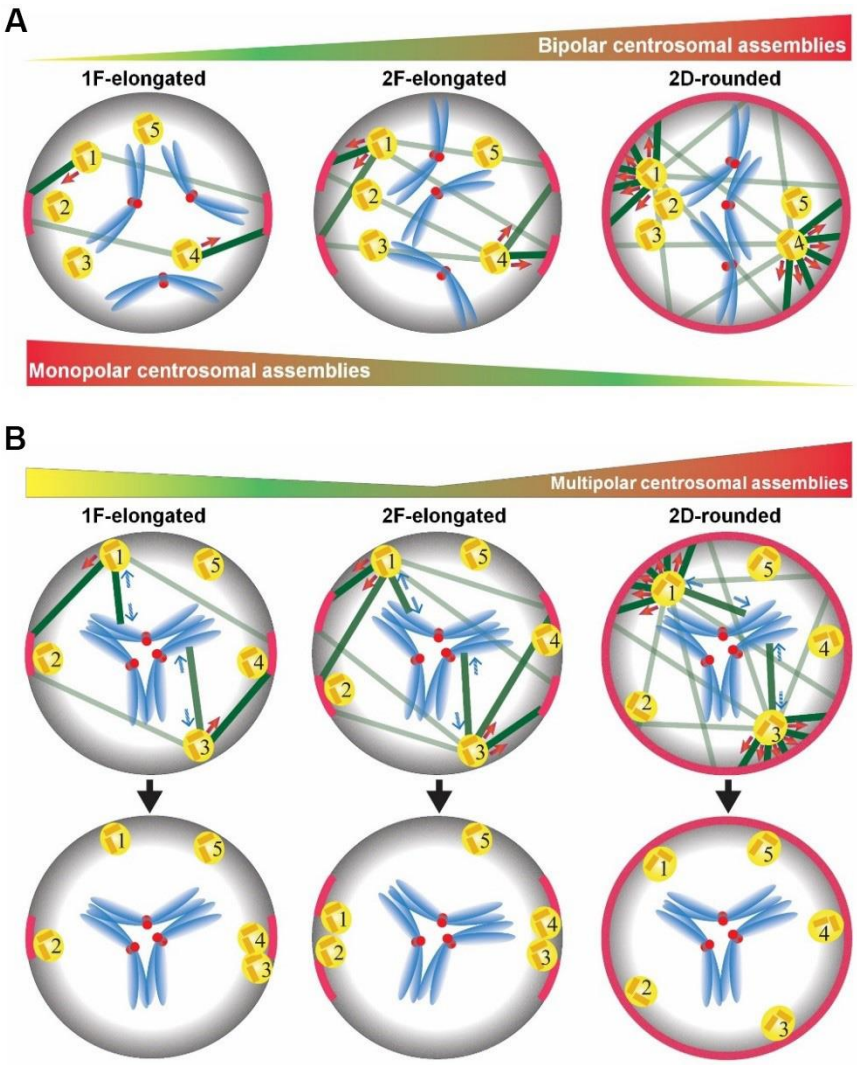

Fig. S9. Schematic diagram explaining the increasing or decreasing trend of (*A*) bipolar, monopolar, and (*B*) multipolar statistics with increasing RF coverage from 1F→2F→2D. Each centrosome feels strong attraction from the proximal RF spots. Two such CSs (CS 1 and CS 4 in (*A*), and CS 1 and CS 3 in (*B*)), one in each half of the cell, are shown to have strongly connected to the proximal RF spots (dark lines) and weakly to the distal RF spots (light lines). (*A*) With increasing RF coverage, the CSs feel more attraction towards the proximal RF region (denoted by multiple red arrows), leading to an increase (decrease) in the bipolar (monopolar) CS assemblies from 1F to 2D. (*B*) In the multipolar configurations, CSs are also under strong repulsion from the centrally located chromosomes apart from the CS-RF attraction. The tendency of each CS to move towards the proximal RF-spots is higher in the 2F-elongated case than in the 1F-elongated scenario. In contrast to the 1F-elongated example, where CS 3 is shown to reach the proximal RF spot despite chromosomal repulsion, two CSs (CS 1 and CS 3) are shown to reach the RF spots in the 2F-elongated case due to comparatively stronger attraction from two proximal RF spots. Because of the proximity of the RF spots, neighboring CSs merge via inter-centrosomal attractions. The CSs in the 2D rounded scenario are strongly attracted from the surrounding RF band, resulting in the highest proportion of multipolarity compared to other cases.

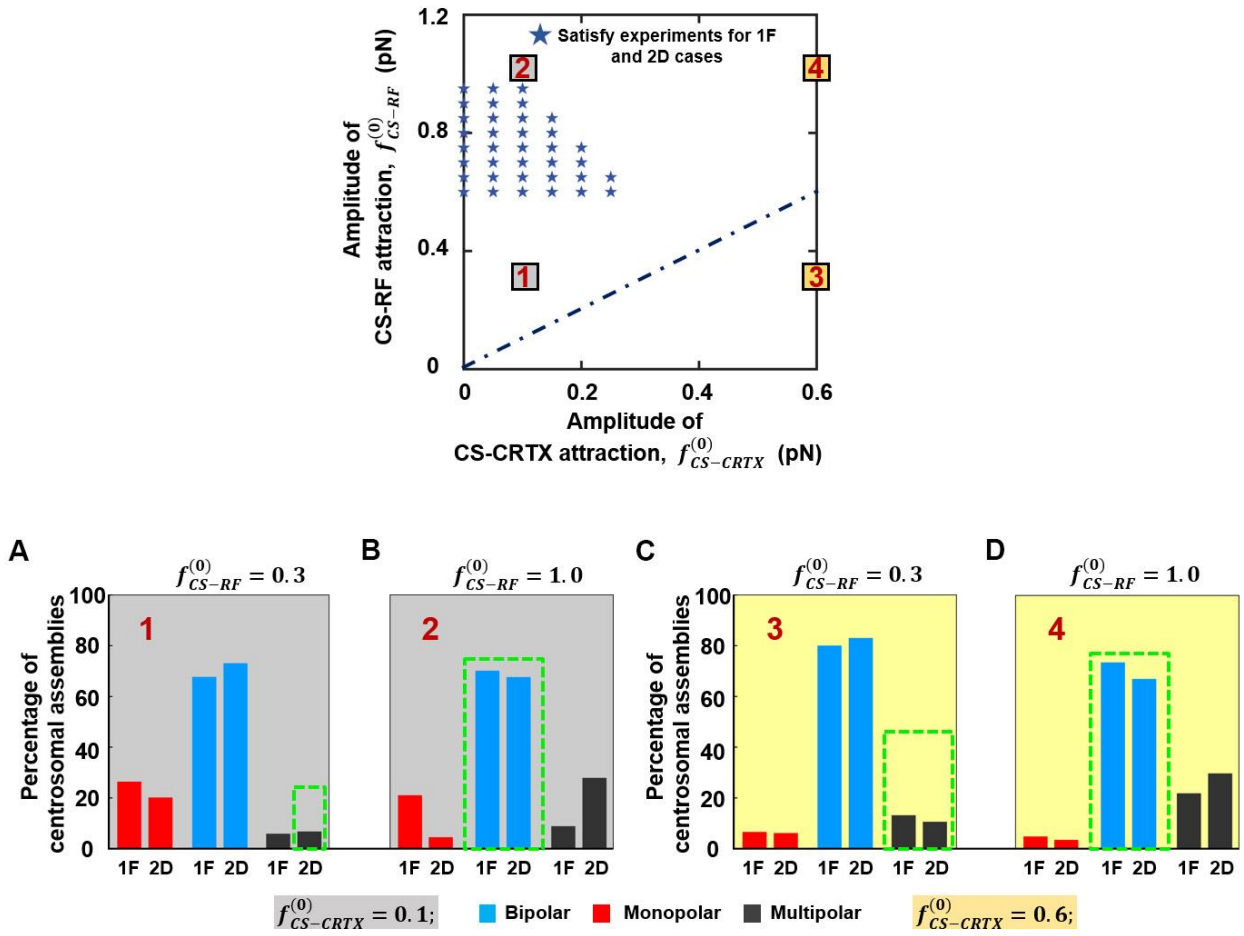

Fig. S10. Spindle statistics in the experimentally conflicting parameter regime. (*A*) The bar plot shows the statistics of monopolar, bipolar, and multipolar spindles at weak CS-CRTX attraction when the amplitude of CS-RF attraction is less (region 1 with CS-RF attraction > CS-CRTX attraction) or (*B*) greater (region 2 with CS-RF attraction >> CS-CRTX attraction) than the experimentally consistent CS-RF attraction. For the 2D-rounded case, the percentage of monopolar spindles exceeds the multipolar spindles at smaller CS-RF attraction (region 1), contradicting the experimental findings in **Fig. 4*C*,** main text. (*C*) Spindle statistics with significantly greater CS-CRTX attraction, with CS-RF amplitude less (region 3) and (*D*) more (region 4) than the CS-CRTX attraction. The data contained within the green dashed boxes contradicts the experimental prediction.

Variation of range of interaction between CS-CS and CS-CH:

Altering the range of interactions between CS-CS and CS-CH (denoted by L_1) can substantially change the parameter space that satisfies the experiment for the 1F-elongated and 2D-rounded case (**Fig. S11**). We observed an upward shifting of the parameter regime when L_1 is decreased (short-range). For smaller $L_1$the proportion of monopolarity is greater than the bi/multi polarity [1], which contradicts our experimental findings in **Fig. 4*C*** (see main text). Increased monopolarity at smaller L_1 arises due to weakened repulsion between the CS and CH. For larger L_1, the long-range repulsion among CSs pushes the CSs to the cell surface, increasing the multipolarity.

Besides all other aspects, the proportion of monopolar spindles in the 2D-rounded scenario must be less than the multipolar spindles to satisfy the experimental predictions in **Fig. 4*C*** (see main text). Note that, monopolarity decreases and multipolarity increases in the presence of a strong, attractive force from the cell surface. Since the monopolarity is greater for smaller L_1, larger forces from the retraction fibers are required to obtain the experimentally observed regime in which the multipolarity for the 2D case is greater than the monopolarity (see **Fig. 4*C***, main text). As a result, we observe an upward shift in the experimentally consistent parameter regime for smaller L_1 compared to larger L_1.

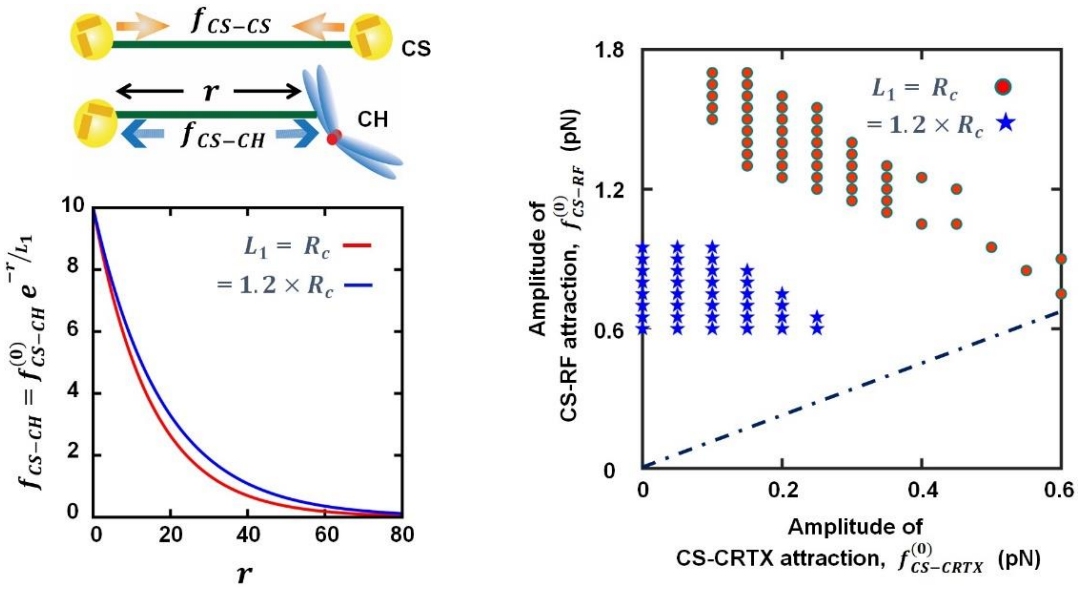

Fig. S11. The spindle outcome depends on the interaction range between the CS-CS and CS-CH pairs. The joint parameter space satisfying the experimental results for the 1F-elongated and 2D-rounded cases with different values of the range of interaction, L_1, between the CS-CS and CS-CH pairs: $L_1 = R_c$ and $1.2 \times R_c$, respectively (right); here, $R_c = 15\ \mu m$ is the cell radius. The nature of the forces acting between one such pair (between CS and CH) is shown (in left) for two different L_1's .

Spindle morphology in the 2F-kite scenario:

Although the RF distribution for the 2F-kite case is not well distinguished from the experiments, we attempt to investigate the spindle outcomes using three distinct RF spots on the cell surface. Two primary spots are positioned orthogonally and the third spot is on the opposite cell surface (**Fig. S12*A***). We uncover that a smaller region around the bottom-right corner of the joint parameter space qualitatively reflects the experimental predictions for all four cases (1F, 2F, 2F-kite, and 2D) (**Fig. S12*B***). Note that, in this small parameter regime, the ratio of the amplitudes of CS-RF attraction to that of the CS-CRTX attraction is not too great (~ 3) as it is on the left of the parameter space. We observe that the changes in the spindle statistics for the 1F-elongated, 2F-elongated, and 2F-kite cases are relatively small within this joint parameter regime (**Fig. S12*C***). These results are primarily attributed to the fact that in this parameter range, due to the relatively

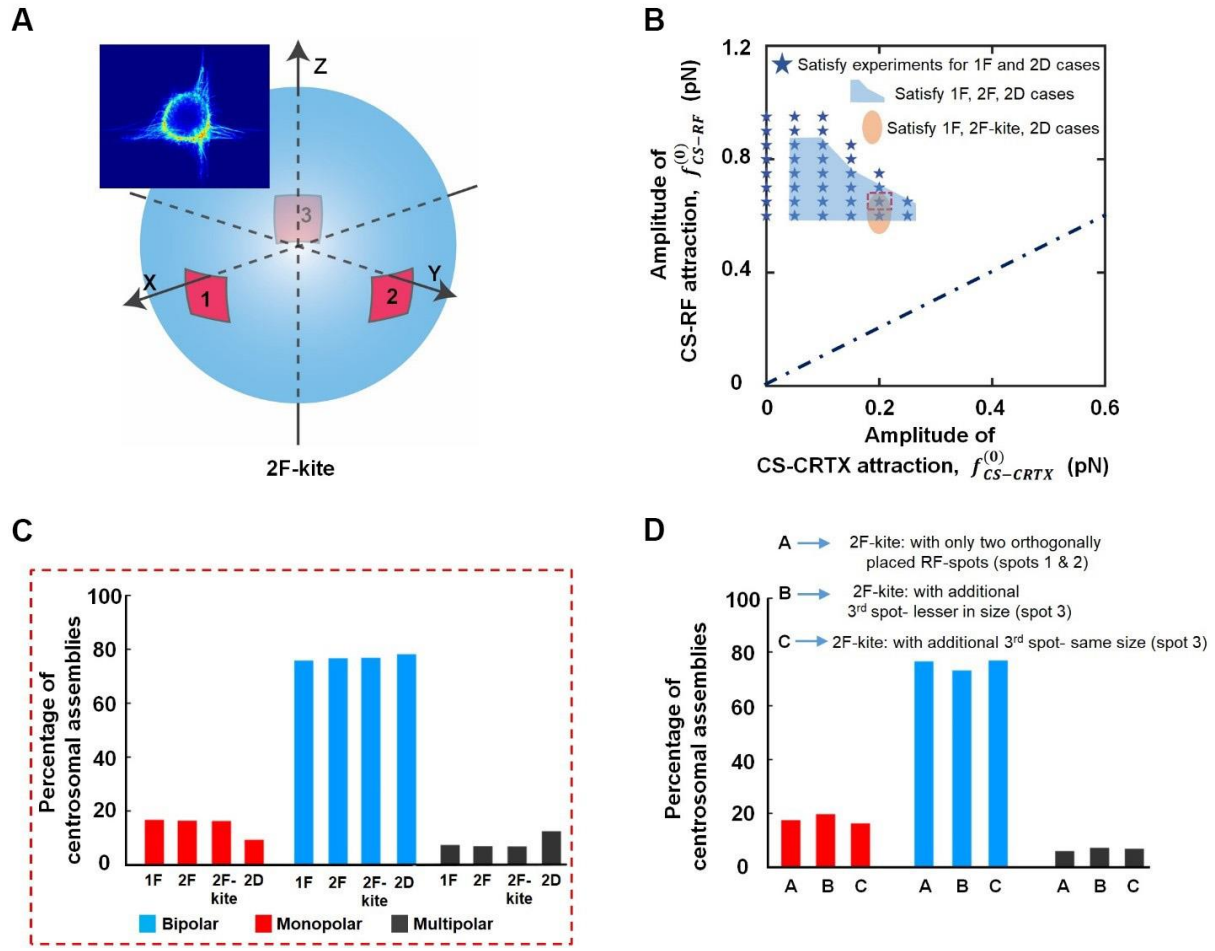

Fig. S12. Spindle outcomes with 2F-kite case. (*A*) The shape and position of the RF-spots considered for the 2F-kite cases in the simulations based on the experimentally observed RF distribution. (*B*) A smaller region around the bottom-right corner of the joint parameter space qualitatively reflects the experimental predictions for all four cases (1F, 2F, 2F-kite, and 2D). The corresponding statistics of mono-, bi-, and multipolar spindles for one such point is shown in (*C*). Here, the statistics for the 1F, 2F and 2F-kite cases are relatively flat. (*D*) There is no substantial difference in the spindle outcomes when the third RF-spot is reduced in size or vanishes.

small ratio of the CS-RF and CS-CRTX attractions, the spindle outcomes are predominantly driven by the forces from the larger cortical surface (through CS-CRTX attraction), with the RF spots having a minor effect on the spindle outcomes for the 1F-elongated, 2F-elongated, and 2F-kite cases. However, in the 2D case, the presence of a vast rounded RF region drastically alters the spindle statistics compared to the other scenarios (**Fig. S12*C***). Furthermore, changing the size of the third RF-spot in the 2F-kite case has no significant effect on the spindle outcomes (**Fig. S12*D***).

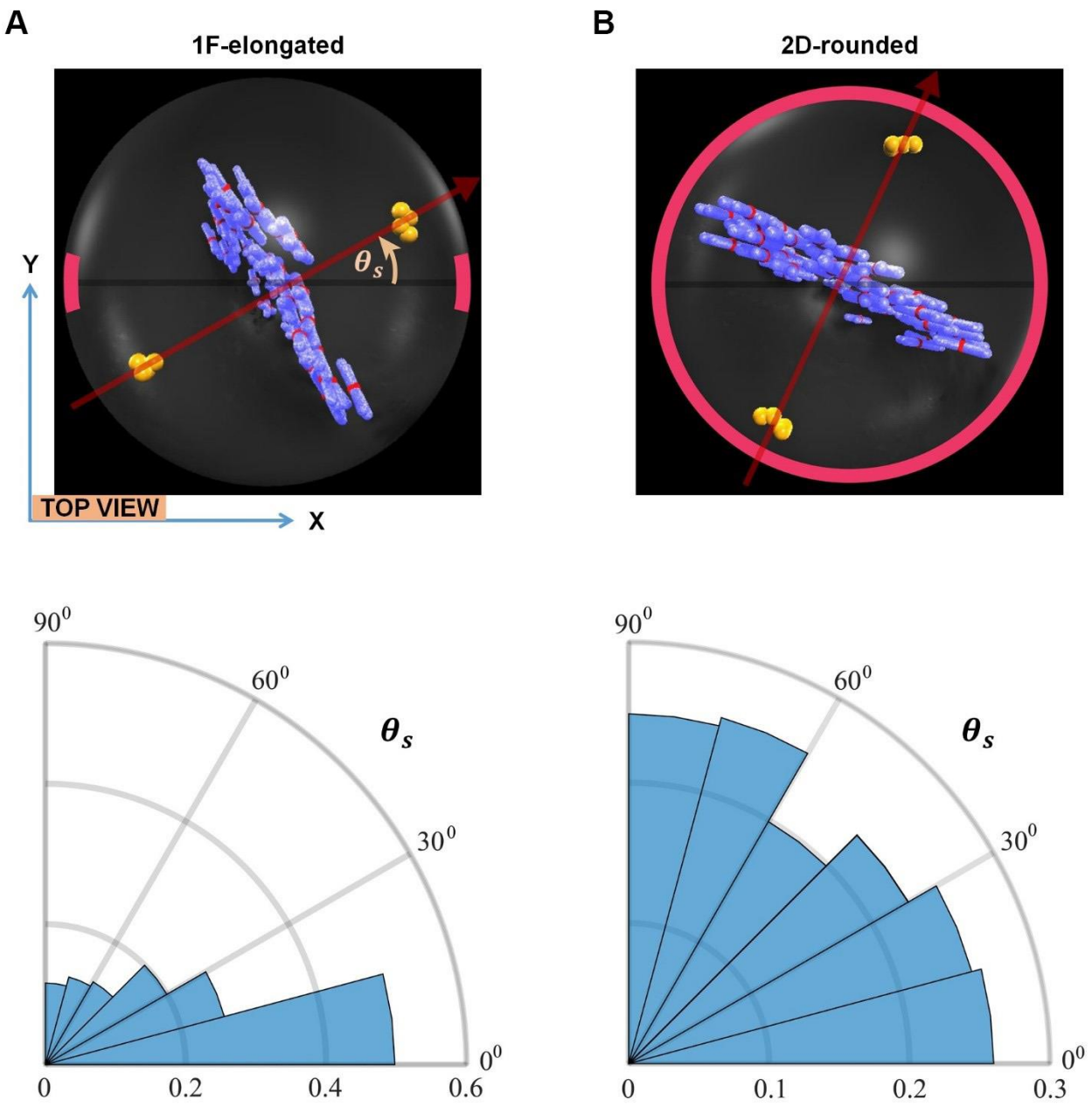

Fig. S13. Spindle axis orientations in 1F-elongated and 2D-rounded cases. Polar histograms of spindle axis orientations (θ_s) for (*A*) 1F-elonagetd and (*B*) 2D-rounded cases, respectively with $f_{CS-CRTX}^{(0)} = 0.1\ pN$ and $f_{CS-RF}^{(0)} = 0.75\ pN$.

COMPUTATIONAL MODEL

The centrosomes (CSs) and chromosomes (CHs) are distributed within a spherical cell with a radius of R_c. We considered a pairwise interaction between the objects [1]. The forces under consideration are conservative; thus, each pairwise interaction corresponds to potential energy. The entire cell surface is divided into parts where RF zones form on the cell surface under the influence of external fibers, and the remaining regions are devoid of RF patches.

A. Construction of RF-spots on the cell surface

Following the experimental findings, the RF spots on the cell surface are constructed in our computational model (**Fig. 4*D*,** main text). The cell is parameterized by $R_c, \theta,$ and φ. $\theta\ (\in 0, 180^0)$ signifies the polar angle, with $\theta = 0$ denoting a point on the $z-$ axis, and $\varphi\ (\in 0, 360^0)$ denotes the azimuthal angle, with $\varphi = 0$ denoting a point on the $x-$ axis. Each RF-spot with an annular width of $d\theta = d\varphi$ is located at different positions on the cell's surface depending on the number of external fibers. RF-zones are located right below the equatorial plane, with θ ranging from 90^0 to $90^0 + d\theta$. In each fiber scenario, the center of the RF-spots at different places on the cell surface is specified with an azimuthal angle φ_0. Hence, the spots would be ranges between $\varphi_0 - \frac{d\varphi}{2}$ to $\varphi_0 + \frac{d\varphi}{2}$. For the 1F-elongated case, we consider two spots: one is centered at $\varphi_0 = 90^0$, another one is on the diametrically opposite cell surface at $\varphi_0 = 270^0$. We consider four spots for the 2F-elongated case: two of them are at $\varphi_0 = 68.5^0$ and 111.5^0. The other two are on the opposite cell surface at $\varphi_0 = 248.5^0$and $\varphi_0 = 291.5^0$. We considered three spots for the 2F-kite scenario (**Fig. S12*A***), two of which are positioned orthogonally at $\varphi_0 = 0^0$ and 90^0. The third is on the other cell sides, at $\varphi_0 = 225^0$. Finally, for the 2D-surface case, the φ ranges from 0 to 360^0, so that a band of RF-spots parallel to the XY – plane is formed right below the equatorial plane.

B. Interactions between pairs of CSs

A dynamically unstable MT emitted by the CS grows isotropically [2–5] and may approach or overlap with MTs emitted by other CSs, generating an effective attractive or repulsive force between the CSs due to the activity of molecular motors interacting with CSs and MTs [6, 7]. The repulsion between the CSs is a vital force responsible for increasing the number of multipolar spindles [1]. The predominance of attractive force is necessary to reduce multipolarity [1]. We introduce an attractive force between each pair of CSs with exponentially decreasing spatial dependence under the assumption of a large number of MTs with an exponential length distribution [2, 8, 9]. The corresponding change in potential energy of shifting one CS away from another CS from a distance r_1 to r_2 is then computed:

$$f_{CS-CS} = f^{(0)}_{CS-CS}\, e^{-r/L_1}, \qquad \Delta E_{CS-CS} = -f^{(0)}_{CS-CS} \int_{r_1}^{r_2} e^{-r/L_1}\, dr. \tag{1}$$

Here, $f^{(0)}_{CS-CS}$ is the amplitude of the force acting between each pair of CSs, *r* is the distance between them, and L_1 denotes the spatial range of interaction between each pair of CSs.

C. Interactions between each CS-KT pairs

The KT-MTs connect the CS to the KT. The molecular motors on the KTs and KT-MTs generate net attractive forces acting between the CS and KT [10]. We consider the simplistic form of a constant, length-independent force [11, 12]: $f_{CS-KT} = f^{(0)}_{CS-KT}$. The respective potential energy of moving either a CS or KT from a distance r_1 to r_2 away from the other one:

$$\Delta E_{CS-KT} = -f^{(0)}_{CS-KT} \int_{r_1}^{r_2} dr \, . \tag{2}$$

D. Interactions between CS-CH pair

A repulsive force is generated between the CS and CH due to the activity of MT polymerization and the molecular motors (chromokinesins: kinesin-10 and kinesin-4) that accumulate at the interface between the chromosomal arms and the microtubule tips that interact with the arms [13–16]. The form of the repulsive force and the respective potential energy read as:

$$f_{CS-CH} = f^{(0)}_{CS-CH}\, e^{-r/L_1} \, , \qquad \Delta E_{CS-CH} = -f^{(0)}_{CS-CH} \int_{r_1}^{r_2} e^{-r/L_1} \, dr. \tag{3}$$

Here, $f^{(0)}_{CS-CH}$ is the amplitude of the force acting between each CS-CH pair, r is the distance between them, and L_1 denotes the spatial range of interaction between each CS-CH pair.

The spatial range of interaction L_1 is kept constant for each CS-CS and CS-CH pair: the underlying assumption is that microtubules of the same average length connect them. In addition, the objects (CS, CH/KT) in three of the above interactions are thought to be point-like. The force vectors act along the center of mass of the objects. The interaction with chromosomal arms is not explicitly considered in our model; instead, a point resembling the center of mass of the chromosome arms is considered to account for the interaction between the CS and CH. We make use of the fact that the center of mass of both KTs and chromosomal arms are close together in the centromeric region of one chromosome. Thus, we employ two force vectors for a single chromosome: one connecting the CS and KT, and the other parallel vector connecting the CS to the respective chromosome arms.

E. Interactions between the CS and the cell cortex

As mentioned earlier, the entire cell surface is divided into two sections: those where the cortical region appears to operate as a hotspot for retraction fibers and those that are free of retraction fibers. When we refer to the “cell cortex”, we mean the parts of the cell surface that lack retraction fibers. The discussions/statements on retraction fiber zones are made explicit in the appropriate locations.

When the astral MTs from the CSs reach the cell cortex, they are reeled in by the molecular motors, causing an attraction on the CS [17–20]. As explained below, the cell cortex is approximated by discrete cortical nodes in the simulations. We utilize the following force expression to account for the attraction between a single CS and a cortical node:

$$f_{CS-CRTX} = f^{(0)}_{CS-CRTX}\, e^{-r/L_2}. \tag{4}$$

Here, $f_{CS-CRTX}^{(0)}$ is the amplitude of the force acting between the CS and the cortical node, r is the distance between them, and L_2 is the spatial range of interaction with the cortex.
The corresponding potential energy of moving a CS from a distance $r_1(\mathbf{s})$ to $r_2(\mathbf{s})$ away from the cortical node point with coordinate **s**, read as:

$$\Delta E_{CS-CRTX} = -\int_{\Omega} d\mathbf{s} \int_{r_1(\mathbf{s})}^{r_2(\mathbf{s})} f_{CS-CRTX}^{(0)} e^{-r/L_2} dr. \quad (5)$$

The integral over the cell cortex Ω becomes the sum over the nodes for discrete cortical nodes.

F. Interactions between the CS and the retraction fibers zone

Astral MTs are more likely to interact with the RF-zones using similar spatially dependent force profiles. However, it is reasonable to expect that the actin-reach retraction fiber regions would interact with astral MTs with a different force amplitude than the rest of the cell cortex. Similar to the force expression used above in Eq. 4, we assume an exponentially diminishing attractive force acting on the CS due to molecular motor activity on the RF-Zones, with a force amplitude $f_{CS-RF}^{(0)}$:

$$f_{CS-RF} = f_{CS-RF}^{(0)} e^{-r/L_2}. \quad (6)$$

The respective potential energy ΔE_{CS-RF}would follow a similar form of Eq. 5:

$$\Delta E_{CS-RF} = -\int_{\Omega'} d\mathbf{s} \int_{r_1(\mathbf{s})}^{r_2(\mathbf{s})} f_{CS-RF}^{(0)} e^{-r/L_2} dr. \quad (7)$$

The integral over the RF attachment regions on the cell surface Ω′ becomes the sum over the discrete surface nodes attached to the RFs.

SIMULATION PROTOCOL

The centrosomes and chromosomes are initially distributed randomly inside a spherical cell of radius $15\ \mu m$. The cell interior is fragmented into a three-dimensional cubic lattice grid with lattice spacing of $1\ \mu m$. The cell surface is discretized into roughly equidistant nodes with grid size comparable to the inside cell. The CSs and CHs are represented by point-like objects. Any particle cannot move to a site that is occupied by any other particles. Between pairs of chromosomes, there is a steric repulsion that scales as the inverse square mutual distance and is active when the mutual distance is less than two units of the numerical grid. CSs and CHs are not permitted to cross the cell border during temporal evolution.
The system is simulated using the Monte-Carlo algorithm. At each Monte Carlo Step, the system is updated in the following manner:

1. A CS or CH is chosen randomly.
2. If the chosen object is CS, then the respective energy change ΔE for moving it from its former position r_1 to a randomly chosen vacant site at the position r_2 is computed by adding ΔE_{CS-CS}, ΔE_{CS-KT}, ΔE_{CS-CH}, $\Delta E_{CS-CRTX}$, and ΔE_{CS-RF}.

3. If it is a CH, then the change in the energy, ΔE, is determined by adding ΔE_{CS-KT} and ΔE_{CS-CH} only. The move to the vacant site is accepted if $\Delta E \leq 0$. Otherwise, the move is accepted with Boltzmann weight $P = e^{-\beta E}$, where E is inversely proportional to the effective temperature required to update the system [21]. The simulation is continued until the system achieves a stable mechanical equilibrium. Two or more CSs are considered clustered in the equilibrium configuration if they are within a distance d_{merge} ($\sim 1.5\ \mu m$, corresponding to when two CSs are in the nearby nodes of the numerical grid). The equilibrium statistics were generated using 1000 − 5000 random initial configurations. The model parameters are noted in TABLE I. More information on simulation details can be found in [1].

TABLE I. **List of parameters used in this work**

Abbreviations	**Meaning**	**Value | Range**
$\boldsymbol{f_{CS-CS}^{(0)}}$	Amplitude of CS-CS attraction	$-1.5\ pN$
$\boldsymbol{f_{CS-KT}^{(0)}}$	Amplitude of CS-KT attraction	$-4.0\ pN$
$\boldsymbol{f_{CS-CH}^{(0)}}$	Amplitude of CS-CH repulsion	$10\ pN$
$\boldsymbol{f_{CS-CRTX}^{(0)}}$	Amplitude of CS-CRTX attraction	0 to $-\ 2\ pN$
$\boldsymbol{f_{CS-RF}^{(0)}}$	Amplitude of CS-RF attraction	0 to $-\ 2\ pN$
$\boldsymbol{R_c}$	Cell radius	$15\ \mu m$
$\boldsymbol{d\theta, d\varphi}$	Annular width of the RF-spots	20^0 | 10^0 to 30^0
$\boldsymbol{L_1}$	Spatial range of CS-CS and CS-CH interactions	$1.2\ \times\ R_c\ \mu m \mid R_c\ to \sim 1.33 \times R_c\ \mu m$
$\boldsymbol{L_2}$	Spatial range of CS-CRTX and CS-RF interactions	$\frac{L_1}{4}\mu m$
$\boldsymbol{d_{merge}}$	Merging distance between centrosomes considered as clustered	$1.5\ \mu m$
$\boldsymbol{\beta}$	Inverse temperature	$20\ (pN\ \times \mu m)^{-1}$

References

1. S. Chatterjee, A. Sarkar, J. Zhu, A. Khodjakov, A. Mogilner, and R. Paul, Mechanics of multicentrosomal clustering in bipolar mitotic spindles, *Biophysical Journal* **119**, 434–447 (2020).

2. F Verde, M Dogterom, E Stelzer, E Karsenti, and S Leibler, Control of microtubule dynamics and length by cyclin A- and cyclin B-dependent kinases in xenopus egg extracts, *J. Cell Biol.* **118**, 1097–1108 (1992).

3. B Lacroix, G Letort, L Pitayu, J Sall´e, M Stefanutti, G Maton, A M Ladouceur, J C Canman, P S Maddox, A S Maddox, N Minc, F N´ed´elec, and J Dumont, Microtubule dynamics scale with cell size to set spindle length and assembly timing, *Dev Cell* **45**, 496–511 (2018).

4. C. G. Pearson, M. K. Gardner, L. V. Paliulis, E. D. Salmon, D. J. Odde, and K. Bloom, Measuring nanometer scale gradients in spindle microtubule dynamics using model convolution microscopy, *Mol Biol Cell* **17**, 4069–79 (2006).

5. R. Paul, R. Wollman, W. T. Silkworth, I. K. Nardi, D. Cimini, and A. Mogilner, Computer simulations predict that chromosome movements and rotations accelerate mitotic spindle assembly without compromising accuracy, *Proc Natl Acad Sci U S A* **106(37)**, 15708–15713 (2009).

6. S. Som, S. Chatterjee, and R. Paul, Mechanistic three-dimensional model to study centrosome positioning in the interphase cell, Phys. Rev. E **99**, 012409 (2019).

7. S. Chatterjee, S. Som, N. Varshney, PVS Satyadev, K. Sanyal, and R. Paul, Mechanics of microtubule organizing center clustering and spindle positioning in budding yeast cryptococcus neoformans, *Phys. Rev. E* **104**, 034402 (2021).

8. S. Sutradhar, S. Basu, and R. Paul, Intercentrosomal angular separation during mitosis plays a crucial role for maintaining spindle stability, *Phys. Rev. E* **92**, 042714 (2015).

9. M. Dogterom and S. Leibler, Physical aspects of the growth and regulation of microtubule structures, *Phys Rev Lett.* **70**, 1347–1350 (1993).

10. A. P. Joglekar and A. A. Kukreja, How kinetochore architecture shapes the mechanisms of its function, *Curr Biol **27***, R816–r824 (2017).

11. R. Dietz, Anaphase behaviour of inversions in living crane-fly spermatocytes, *Chromosom. Today* **3**, 70–85 (1972).

12. N. P. Ferenz, R. Paul, C. Fagerstrom, A. Mogilner, and P. Wadsworth, Dynein antagonizes eg5 by crosslinking and sliding antiparallel microtubules, *Curr Biol.* **19(21)**, 1833–1838 (2009).

13. G. J. Brouhard and A. J. Hunt, Microtubule movements on the arms of mitotic chromosomes: polar ejection forces quantified in vitro, *Proc Natl Acad Sci U S A* **102**, 13903–8 (2005).

14. K. Ke, J. Cheng, and A. J. Hunt, The distribution of polar ejection forces determines the amplitude of chromosome directional instability, *Curr Biol* **19**, 807–15 (2009).

15. A. A. Ye, J. Deretic, C. M. Hoel, A. W. Hinman, D. Cimini, J. P. Welburn, and T. J. Maresca, Aurora A kinase contributes to a pole-based error correction pathway, *Curr Biol* **25**, 1842–51 (2015).

16. D. Drpic, A. J. Pereira, M. Barisic, T. J. Maresca, and H. Maiato, Polar ejection forces promote the conversion from lateral to end-on kinetochore-microtubule attachments on mono-oriented chromosomes, *Cell Rep* **13**, 460–468 (2015).

17. J. C. Waters, R. W. Cole, and C. L. Rieder, The force-producing mechanism for centrosome separation during spindle formation in vertebrates is intrinsic to each aster, *J Cell Biol* **122**, 361–72 (1993).

18. G. Letort, F. Nedelec, L. Blanchoin, and M. Thery, Centrosome centering and decentering by microtubule network rearrangement, *Mol Biol Cell* **27**, 2833–43 (2016).

19. L. Laan, S. Roth, and M. Dogterom, End-on microtubule-dynein interactions and pulling-based positioning of microtubule organizing centers, *Cell Cycle* **11**, 3750–7 (2012).

20. A. Sarkar, R. Paul, and H. Rieger, Search and capture efficiency of dynamic microtubules for centrosome relocation during IS formation, Biophysical Journal **116**, 2079–2091 (2019).

21. E. Ben-Isaac, Y. Park, G. Popescu, F. L. Brown, N. S. Gov, and Y. Shokef, Effective temperature of red-blood-cell membrane fluctuations, *Phys Rev Lett* **106**, 238103 (2011).

Movie Legends

Movie S1: HeLa cell expressing Histone H2B GFP dividing on a single fiber (timestamp-h:min) and scale bar 20 µm.
Movie S2: HeLa cell expressing Histone H2B GFP dividing on a orthogonal arrangement of fibers (timestamp-h:min) and scale bar 20 µm.
Movie S3: HeLa cell expressing Histone H2B GFP dividing on a fiber doublet (timestamp-h:min) and scale bar 20 µm.
Movie S4: HeLa cell expressing Histone H2B GFP dividing on multiple fibers (timestamp-h:min) and scale bar 20 µm.
Movie S5: HeLa cell expressing Histone H2B GFP dividing on flat glass coverslips (timestamp-h:min) and scale bar 20 µm.
Movie S6: High-speed recording of division event of Hela cell on single fibers, showing movements of the rounded cell during metaphase (timestamp-h:min:sec) and scale bar 20 µm.
Movie S7: High-speed recording of division event of Hela cell on crossing fibers (timestamp-h:min:sec) and scale bar 20 µm.
Movie S8: High-speed recording of division event of Hela cell on a fiber doublet (timestamp-h:min:sec) and scale bar 20 µm.
Movie S9: High-speed recording of HeLa division on multiple fibers (timestamp-h:min:sec) and scale bar 20 µm.
Movie S10: Metaphase plate (MP) oscillations over the course of mitosis for HeLa cell dividing on a single fiber. Red arrow is included in the GFP channel for visual tracking of the MP oscillations (timestamp-h:min) and scale bar 20 µm.
Movie S11: Metaphase plate (MP) oscillations for HeLa cell dividing on crossing fibers (timestamp-h:min) and scale bar 20 µm.
Movie S12: Metaphase plate (MP) oscillations for HeLa cell dividing on fiber doublets (timestamp-h:min) and scale bar 20 µm.
Movie S13: Reduced level of metaphase plate (MP) oscillations for HeLa cell dividing on multiple fibers (timestamp-h:min) and scale bar 20 µm.
Movie S14: Simulation movies demonstrating the formation of a monopolar spindle in the 2D-rounded case. CSs are yellow, chromosome arms are blue, KTs are red. The region between two circular rings (colour: orange) at the equatorial area represents the RF-band.
Movie S15: Simulation movies demonstrating the formation of a bipolar spindle in the 2D-rounded case. CSs are yellow, chromosome arms are blue, KTs are red. The region between two circular rings (colour: orange) at the equatorial area represents the RF-band.
Movie S16: Simulation movies demonstrating the formation of a multipolar spindle in the 2D-rounded case. CSs are yellow, chromosome arms are blue, KTs are red. The region between two circular rings (colour: orange) at the equatorial area represents the RF-band.